Energy &
Environmental
Science

Accepted Manuscript

This article can be cited before page numbers have been issued, to do this please use: S. Qu, F. Yang, H. Huang, Y. Li, C. Sun, Q. Zhang, S. Du, L. Yan, Z. Lan, Z. Wang, T. Jiang, P. Cui, X. Ai and M. Li, *Energy Environ. Sci.*, 2025, DOI: 10.1039/D4EE05319B.

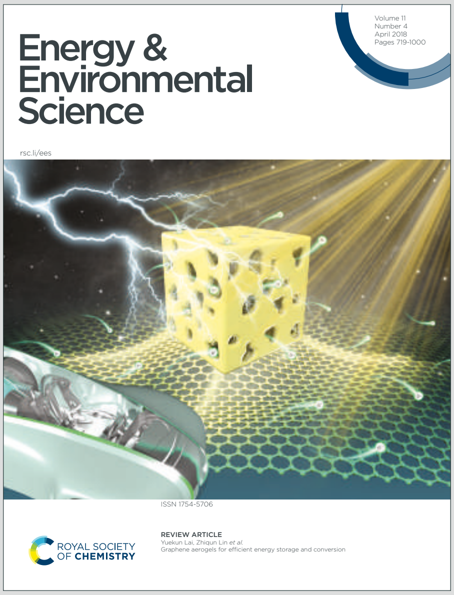

ROYAL SOCIETY
OF CHEMISTRY

rsc.li/ees

View Article Online
DOI: 10.1039/D4EE05319B

Broader context:

Inverted perovskite solar cells (PSCs) have garnered significant attention due to their remarkable compatibility in tandem solar cells. As an inorganic p-type semiconductor, NiO_X is commonly served as the hole transport materials for advancing inverted PSCs towards commercialization, leveraging its scalability and cost-effectiveness. However, the presence of surface defects and undesired interface chemical reactivity hinder the enhancement of device stability. In this work, we utilized the methylene blue (MB) to be co-absorbed with [4-(3,6-dimethyl-9H-carbazol-9-yl)butyl]phosphonic acid (Me-4PACz) as a functionalized interfacial layer. We revealed that the MB can mitigate the uneven disperse of Me-4PACz on NiOx surface, which reduces the voids and aggregates, providing a flattened and compact interfacial layer. Moreover, the MB can serve as a redox mediator to selectively reduce high-valence state of Ni species and oxidize metallic Pb^0, while synergistically passivating interfacial defects through constructing a bridge-link structure, which stabilizes the buried interface. As a consequence, the inverted 0.08 cm^2-PSCs and 1 cm^2-PSCs achieved PCEs of 26.39% and 24.89%, respectively. The device showed enhanced stability, retaining 90% of its initial PCE after 1500 hours of operation under 1-sun illumination. Our work presents a feasible route to enhance device stability through optimizing and functionalizing the interfacial layer.

View Article Online
DOI: 10.1039/D4EE05319B

ARTICLE

Redox mediator-modified self-assembled monolayer stabilizes buried interface in efficient inverted perovskite solar cells

Received 00th January 20xx,
Accepted 00th January 20xx

DOI: 10.1039/x0xx00000x

Shujie Qu[a], Fu Yang[a], Hao Huang[a]*, Yiyi Li[b], Changxu Sun[a], Qiang Zhang[a], Shuxian Du[a], Luyao Yan[a], Zhineng Lan[a], Zhiwei Wang[a], Tongtong Jiang[a], Peng Cui[a], Xicheng Ai[b], Meicheng Li[a]*

Abstract: Utilizing self-assembled monolayer (SAM) of [4-(3,6-Dimethyl-9H-carbazol-9-yl)butyl]phosphonic acid as the interfacial layer on NiO_x (Me-4PACz) has been proven to be a feasible approach to improve photovoltaic performance of inverted perovskite solar cells (PSCs). However, considering the chemical reactivity of the NiO_x surface and inhomogeneous SAM, interface stability is still an urgent issue that needs to be addressed. Here, methylene blue, a redox molecule, is co-absorbed with Me-4PACz to serve as a functionalized interfacial layer, which effectively enhances the interface stability. The methylene blue can serve as a redox mediator to selectively reduce the high-valence state of Ni species and oxidize metallic Pb^0, suppressing the undesired interfacial reaction and reducing the interfacial defects. Besides, the methylene blue can also mitigate the uneven disperse of Me-4PACz through forming a π–π interaction, which reduces the voids and aggregates, providing a flattened and compact interfacial layer. These effects enable the inverted 0.08 cm^2-PSCs and 1 cm^2-PSCs to achieve an efficiency of 26.39% and 24.89% respectively. Encouragingly, the device possesses enhanced stability even under harsh damp-heat conditions, retaining 91% of its initial efficiency after 1500 hours of UV irradiation, and also retaining 90% of its initial efficiency after 1500 hours of operation under 1-sun illumination.

Introduction

Metal halide perovskite solar cells (PSCs), as a transformative technology in the field of photovoltaics, stand as a promising candidate for efficient conversion of solar energy, achieving tremendous progress in power conversion efficiency (PCE) with a certificated value exceeding 26% [1]. Notably, the inverted PSCs have received huge attention due to their advantages of simplified fabrication, greater amenability to charge extraction layers, and compatibility in tandem solar cells [2-7]. In the past three years, the efficiency of inverted PSCs has made rapid progress, which mainly results from the massive research on the hole transport layer (HTL) materials and the buried interface. Among the HTL materials, NiO_x, an inorganic p-type semiconductor, is commonly utilized due to its cost-effectiveness and scalability [8-9]. However, the presence of surface defects, mismatched energy levels with perovskite, and undesired interface chemical reactivity bring a hindrance to achieve high-efficiency inverted PSCs with excellent stability.

The variety of high-oxidative-state Ni species on the surface of NiO_x makes the surface chemistry of the NiO_x layer complicated, resulting in the perovskite decomposition through diverse chemical reactive between NiO_x and perovskite at the hetero-interface [10-11]. It is reported that detrimental reaction between $Ni^{>3+}$ and organic cation of perovskite induce A-site-defective defects at the interface of NiO_x/perovskite, and the reaction between $Ni^{>3+}$ and I^- of perovskite induce I_2 and I_3^-which limits the efficiency improvement and stability enhancement of NiO_x-based PSCs [12-13]. Considering the undesired interface chemical reactivity, mismatched energy levels with perovskite, and interfacial defects, various strategies have been developed to modify the NiO_x/perovskite interface, such as the utilization of organic additives, buffer layers, and inorganic salts [14-16]. Among these strategies, using self-assembled monolayers (SAM) has been brought into the spotlight as its distinct advantage of promoting interfacial carrier transport. At present, phosphonic acid SAMs with a carbazole core are the star material, enabling performance advances of inverted PSCs through serving as the the interfacial materials at the NiO_x/perovskite interface [17-18]. For example, [4-(3,6-dimethyl-9H-carbazol-9-yl)butyl]phosphonic acid (Me-4PACz) has been utilized to construct a buffer layer at the NiO_x/perovskite interface, which can optimize the energy level between NiO_x and $FAPbI_3$ (FA is Formamidine) [17]. However, although these SAMs have been employed to modify the NiO_x/perovskite interface, the attainment of high-density, closely packed SAMs remains challenging, resulting in inhomogeneous distribution and the accordingly undesired aggregates [19-22]. Moreover, although the utilization of SAMs as the buffer layer at the NiO_x/perovskite interface can help to mitigate the interfacial reactivity [23-24], the potential impact of NiO_x on the perovskite stability still exists, especially considering the inhomogeneous

---

[a] *State Key Laboratory of Alternate Electrical Power System with Renewable Energy Sources, North China Electric Power University, Beijing 102206, China*
[b] *Key Laboratory of Advanced Light Conversion Materials and Biophotonics, School of Chemistry and Life Resources, Renmin University of China, Beijing 100872, China*

Supplementary Information available: [details of any supplementary information available should be included here]. See DOI: 10.1039/x0xx00000x

View Article Online
DOI: 10.1039/D4EE05319B

disperse of SAM materials. Therefore, it is highly desirable for a strategy to collaboratively optimize the SAM deposition and suppress undesired interfacial reactions, further leading to a high-efficiency inverted PSCs with enhanced stability.

Herein, we utilize methylene blue (MB) to be co-absorbed with Me-4PACz to serve as a functionalized interfacial layer, attempting to optimize and stabilize the buried interface. Our research proved that the methylene blue can mitigate the uneven dispersal of Me-4PACz on the NiO$_x$ surface, which reduces the voids and aggregates, providing a flattened and compact buried interface. After co-absorbing methylene blue, the conductivity of the interfacial layer is also increased, contributing to the accelerated interfacial carrier transport. Moreover, the methylene blue can serve as a redox mediator to selectively reduce the high-valence state of Ni species and oxidize metallic Pb^0, while synergistically passivating interfacial defects through constructing a bridge-link structure, which effectively enhances the stability of the buried interface. These advantages translate to the improved efficiency and enhanced stability of inverted PSCs, in which the inverted PSCs with an aperture area of 0.08 cm^2 achieve a PCE of 26.39% and the inverted PSCs with an aperture area of 1 cm^2 achieve a PCE of 24.89%. Furthermore, the device can retain 91% of its initial PCE after 1500 hours of UV irradiation in a N$_2$-glovebox, and also retain 90% of its initial PCE after 1500 hours of operation under 1-sun illumination.

Results and discussion

Modified interfacial layer

It is reported that undesired chemical reaction between NiO$_x$ and perovskite badly influence the interface stability, and the interface stability can also be influenced by the inhomogeneous disperse of SAM and the interfacial defects. Considering the suitable redox ability that may reduce Ni$^{>3+}$ and oxidize the Pb^0, and molecular configuration that can form a π–π interaction with SAM and passivate interfacial defects, the MB was chosen to modify the interfacial layers, attempting to enhance the interface stability. We attempted to utilize the MB (molecular structure shown in Supplementary Fig. 1), a redox molecule with the cation possesses variable valences, to modify the SAM (Me-4PACz) interfacial layer at the buried interface in inverted p-i-n PSCs (schematic diagram of device structure shown in Supplementary Fig. 2), and the anion of Cl- is reported to be positive on passivating the interface defects [25-27]. In the following discussion, the sample with Me-4PACz interfacial layer was named as normal, and the sample with Me-4PACz & MB as interfacial layer was named as target, where the optimal amounts of MB was preliminarily determined through experimental exploration (Supplementary Fig. 3 and Supplementary Note S1). Before exploring the influence of MB on the property of interfacial layer, the X-ray Photoelectron Spectroscopy (XPS) characterization was employed to confirm the steady co-absorbance of MB molecule on NiO$_x$ surface along with Me-4PACz, evidenced by a distinct S 2p signal with a peak area ratio of P 2p to be approximately 1:3 (Figure 1a, Supplementary Fig. 4) [28]. We then sought to explore the changes of the surface energy levels of the SAM layer. Ultraviolet photoelectron spectroscopy (UPS) revealed that the SAM shows a negative shift in the Fermi level from -4.46 eV to -4.67 eV (Figure 1b) after incorporating MB [29-30]. This negative shift of the Fermi level was also validated by results of Kelvin probe force microscopy (KPFM), in which the surface potential of target layer was higher than that of control layer (Figure 1c) [31]. The corresponding atomic force microscope (AFM) images were shown in Supplementary Fig. 5. The decreased Fermi level induced by the MB is supposed to promote interfacial hole transport. In addition, Conductive atomic force microscopy (C-AFM) was employed to assess the conductivity of SAM. As shown in Figure 1d, the average surface current of the target layer is 6.81 nA, significantly higher than the 3.53 nA of the normal layer, indicating an improved surface conductivity [32]. To characterize the surface distribution of SAM on NiO$_x$, we employed the advanced Nano-FTIR (Fourier transform infrared) technique, with its schematic structure and mechanism depicted in Supplementary Fig. 6. The extracted data focused on tracking the characteristic stretching vibration of the P=O bond at 1176 cm^{-1}. [33-34] In Figures 1e and 1f, the colors represent the magnitude of the photo-induced surface potential. The normal SAM exhibits a red-green alternating pattern, indicating a non-uniform distribution of SAM with discrete regions. In contrast, the target SAM predominantly displays a red color, indicating a more homogeneous dispersion and optimized coverage of SAM on NiO$_x$ surface [35]. The improved homogeneity of SAM disperse on NiO$_x$ should attribute to the formed π–π interaction between SAM and MB, which weakens the intermolecular forces among SAM molecules and increases the dipole moment of SAM molecule, further helping distribute the SAM and suppress SAM aggregate (Supplementary Fig. 7-10) [36-37].

We hypothesize that the interfacial modification by MB molecules also contributes to interface passivation, considering MB molecule possess two electronegative atoms validated by the calculated surface electrostatic potential (Supplementary Fig. 11). These electronegative atoms of N and S possess long-pair electrons, which potentially can interact with metal atom in NiO$_x$ and perovskite, respectively. DFT calculation was employed to reveal the interfacial interaction between MB with NiO$_x$ and MB with perovskite, respectively. The optimized structure model shows that the N atom in MB electronegative preferentially attaches to NiO$_x$, and the S atoms in MB act as passivating agents to interact with the Pb atom at the buried interface. The calculated adsorption energy of MB at the interface between NiO$_x$ and the perovskite is -12.04 eV, indicating a strong interaction of MB at the buried interface (Figure 1g). To experimentally explore the interaction between MB and NiO$_x$, the Fourier-transform infrared (FTIR) spectroscopy was utilized to reveal a shift of -C=N- group in MB from 1695 cm^{-1} to 1686 cm^{-1} after it was spin-coated on NiO$_x$ surface (Supplementary Fig. 12). Additionally, to experimentally characterize the interaction between MB and perovskite, we used a previously reported method (Supplementary Fig. 13) to expose the bottom surface of the perovskite film with UV-curable adhesive, followed by XPS characterization [38]. As

View Article Online
DOI: 10.1039/D4EE05319B

shown in Figure 1h, compared to normal film, the Pb 4f peaks in target film shift to lower binding energies, indicating the decreased oxidation state of Pb^{2+}, which is related to the formation of complexes between S and the under-coordinated $[PbI_6]^{4-}$. A similar shift was also observed in the I 3d peaks, validating the interaction between MB with perovskite at buried interface (Supplementary Fig. 14). This interaction between MB and perovskite is expected to passivate the perovskite defects, which can be partially validated by the slight improvement of PSCs efficiency when directly incorporating the MB into perovskite precursor (Supplementary Fig. 15). These results suggest that MB can be served as a passivator at the buried interface, which is beneficial to reducing the interfacial carrier loss and enhancing the interface stability [39-41].

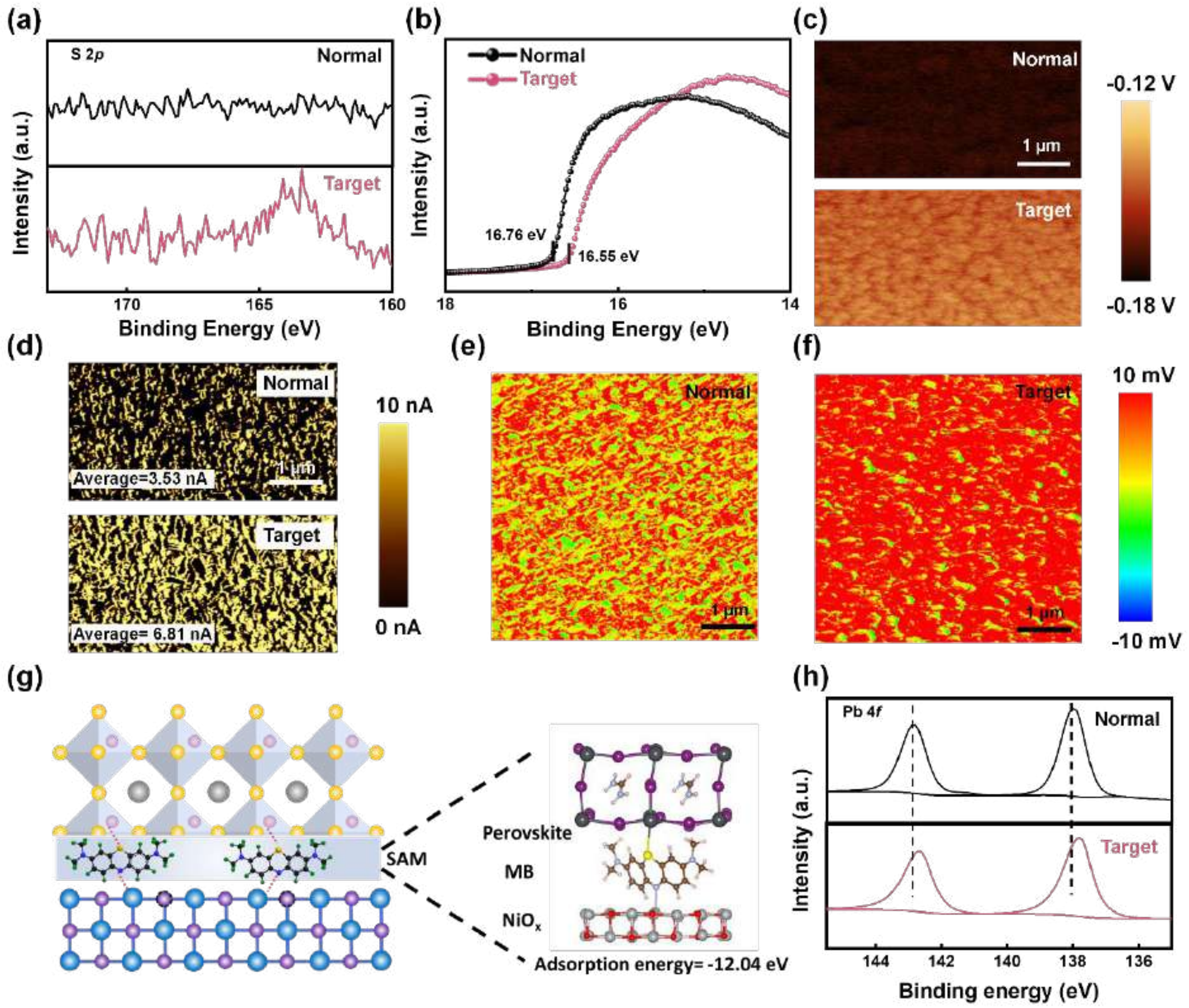

Fig. 1. Modification and Functionalization of MB in SAM. (a) S 2p spectra of the normal and target SAM. (b) UPS spectra of the normal and target SAM. (c) KPFM image of the normal and target SAM. (d) C-AFM image of the normal and target SAM. (e, f) Nano-FTIR image of the normal and target SAM. (g) DFT calculation of MB in interface. (h) Pb 4f spectra of the normal and target perovskite film (buried interface).

Optimized perovskite crystallization and promoted interface hole transport

The co-absorbed MB molecules effectively modify the dispersal of SAM on the NiO_x surface, yielding a flat and compact interfacial layer, which is expected to positively influence the perovskite crystallization. First, scanning electron microscopy (SEM) was employed to evaluate the surface morphology of perovskite films on different substrates. As depicted in Figures 2a and 2b, compared to perovskite film deposited on normal SAM, the perovskite film deposited on the target SAM exhibits significantly optimized morphological characteristics, manifested as a denser, smoother surface with lightly increased grain size [42-43]. Additional AFM images (Supplementary Fig. 16) further confirm this result. Additionally, we characterized the bottom surface of the perovskite films by peeling them off using a UV-curable adhesive method, which we had previously employed when analyzing the bottom surface using XPS. As illustrated in Figure 2d, the bottom surface of the perovskite film deposited on target SAM exhibits a smooth, void-free morphology, whereas the perovskite films deposited on normal SAM (Figure 2c) display numerous voids at the bottom surface. X-ray diffraction (XRD) was further conducted to characterize the crystallinity of the perovskite films with the results shown in Figure 2e. Both films exhibit a (100)/(200) preferred orientation, with corresponding peak positions at approximately 14° and 28°, respectively [44]. In detail, the

View Article Online
DOI: 10.1039/D4EE05319B

perovskite film deposited on the target SAM displays superior crystallinity, which also be validated by the results of grazing-Incidence wide angle X-ray scattering (GIWAXs) (Supplementary Fig.17). The optimized perovskite crystallization is beneficial for achieving high-quality perovskite films with reduced defects. We fabricated hole-only devices to estimate the defect density of the perovskite films using space-charge-limited current (SCLC) measurements (Figure 2f). The trap-filled limit voltage (V_{TFL}) is a critical parameter for evaluating defect density in materials [45]. The defects density (N_{trap}) of the films was calculated according to the formula $N_{trap} = 2\epsilon_r\epsilon_0 V_{TFL}/eL^2$, where ϵ_r is the relative permittivity, ϵ_0 is the vacuum permittivity, e is the electronic charge, L is the thickness of the perovskite film (Supplementary Fig. 18). The target device's V_{TFL} is 0.61 V, giving a N_{trap} of 9.10×10^{15} cm^{-3}, while the normal device's V_{TFL} s 0.86 V, giving a N_{trap} of 1.28×10^{16} cm^{-3}. The reduced defect density of perovskite film may result from the passivated interfacial defects and optimized perovskite crystallization.

After characterizing the perovskite films on different SAM substrates, we also explored the interfacial carrier transport dynamic using photoluminescence (PL) mapping and time-resolved photoluminescence (TRPL) techniques [46-47]. Firstly, the PL mapping results (Figure 2g) demonstrate that the PL intensity of the perovskite films on the target SAM is significantly lower compared to those on the normal SAM, suggesting more efficient hole extraction. The TRPL data, as shown in Figures 2h and 2i, reveals that the perovskite film on target SAM layers exhibits a smaller average lifetime (τ_{avg}) of 57.71 ns compared to 86.51 ns for the perovskite film on normal SAM layers. The τ_{avg} is calculated using the formula $\tau_{avg} =(A_1*\tau_1^2+A2*\tau_2^2)/(A_1*\tau_1+A2*\tau_2)$, where A_1 and A_2 are the amplitudes, and τ_1 and τ_2 are the lifetimes obtained from biexponential fitting. The reduced average carrier lifetime also indicates the promoted interfacial hole extraction. To further explore efficacy of the MB in inverted PSCs, TPV (transient photovoltage) and TPC (transient photocurrent) techniques were employed to measure charge transport and recombination lifetime, respectively [48]. As shown in Supplementary Fig. 19, the photovoltage decay time increased from 8.89 μs in the control PSCs to 26.24 μs in the target PSCs, indicating a longer charge recombination lifetime. This extended carrier lifetime in the target PSCs suggests that defect-assisted charge recombination is suppressed. The TPC decay curves reveal a shorter charge extraction time of 0.89 μs in the target device, indicating faster-photogenerated carrier extraction, which is consistent with TRPL results. Overall, the TPC and TPV measurements confirm that the SAM incorporated with MB can effectively promote interfacial charge carrier extraction, reducing hole accumulation and recombination losses at the buried interface.

View Article Online
DOI: 10.1039/D4EE05319B

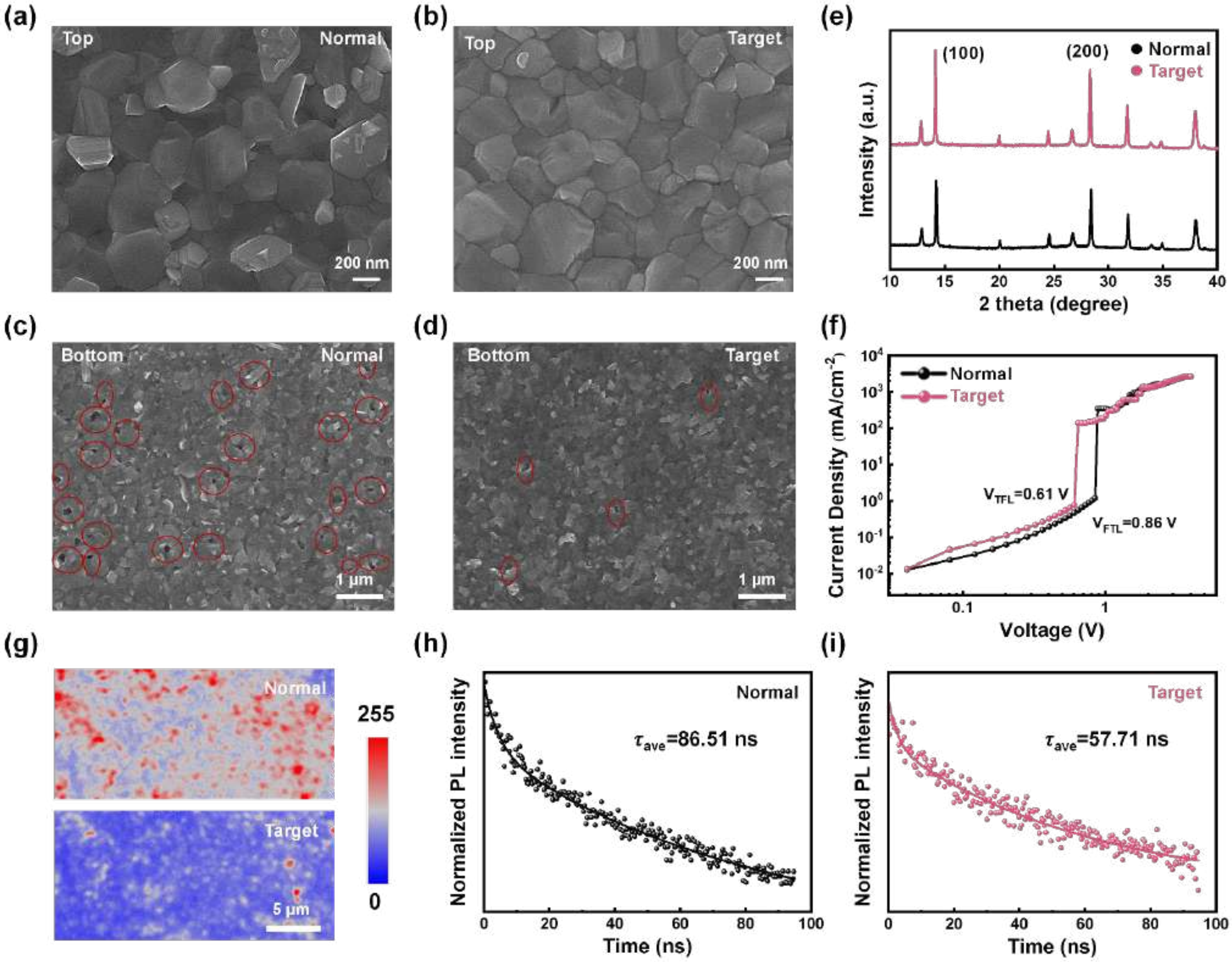

Fig. 2. Improvement in Perovskite Film Deposition and Interfacial Transport Properties. (a, b) SEM image of perovskite film on the normal and target SAM (Top). (c, d) SEM image of perovskite film on the normal and target SAM (Bottom). (e) XRD spectra of the normal and target perovskite film. (f) Dark *J-V* curves of hole-only devices with various SAMs. (g) PL mapping images of the normal and target perovskite film. (h, i) TRPL spectra of perovskite film on the normal and target SAM.

Suppressed interfacial redox reactions

We now turn to discuss the suppressed interfacial detrimental reaction. The variety of Ni species is reported to induce the redox reaction with perovskite, decomposing the perovskite at the NiO_x/perovskite interface. Detailly, the under-coordinated metal cation sites ($Ni^{>3+}$) act both as a Lewis acid or oxidant, resulting in the deprotonation of cation and I^- oxidation. (Figure 3a). The MB molecule contains multiple nitrogen atoms and aromatic rings, which can accept electrons and provide electrons to other materials, making itself redox. The MB also possesses a variety of valance, presenting +1 and +2. We speculate that the MB can serve as an interfacial redox mediator, meaning that the MB can selectively reduce high-valence-states Ni species ($Ni^{>3+}$) and also oxidize metallic Pb^0, preventing the harmful interface reaction and stabilizing the interface (Figure 3a). To explore the redox reaction between high-valence states of Ni species ($Ni^{>3+}$) and MB molecular, we carried out measurement of XPS to characterize the valence states of Ni species covered by SAM or SAM with MB. The Ni $2p_{3/2}$ spectra were deconvoluted referring to the previous articles [12]. As shown in Figure 3b, the peaks located at 854.35, 856.12, and 858.75 eV correspond to Ni^{2+}, Ni^{3+}, and Ni^{4+}, respectively. After incorporating the MB into the SAM, the captured Ni^{4+} species is obviously reduced, indicating the redox

View Article Online
DOI: 10.1039/D4EE03319B

reaction between the Ni^{4+} and MB. This reduced Ni^{4+} species in the control film can also validated by the changes in absorption spectra in Figure 3c. To amplify this redox reaction, we performed UV–ozone (UVO) surface treatment, a method to oxidize the low-valence-states Ni species and then increase the Ni^{4+} species, to make the formerly transparent NiO_x film to be a semitransparent film with a light black color (Supplementary Fig. 20) [49]. After coating SAM with MB, a bleaching effect of UVO-treated NiO_x film can be observed, confirming the reduced Ni^{4+} species through redox reaction with MB. To conform the oxidation of MB on Pb^0, we firstly performed a measurement of cyclic voltammetry (CV) to characterize the redox potential of MB. As illustrated in Supplementary Fig. 21, The redox potential of MB, referenced to the normal hydrogen electrode (NHE), lies between that of Pb (-0.365 V vs. NHE) and I_2 (0.536 V vs. NHE), indicating that MB can selectively oxidize Pb^0. Subsequently, we carried out XPS measurements on perovskite films with and without MB. Before spin-coating, both precursors were aged under UV irradiation for 12 hours to amplify the effect of MB on oxidizing Pb^0. As shown in Figure 3d, in the Pb 4f spectra, there are two additional peaks centered on 141.10 eV and 136.21 eV, which are corresponded to Pb^0 resulting from the decomposition of PbI_2 under UV irradiation. In comparison, the Pb^0 cannot be detected on the film with MB, indicating that the Pb^0 can be eliminated by MB through redox reaction [50-51]. The XPS measurement was also performed on films, PbI_2, PbI_2 with MB, PbI_2 with Me-4PACZ, respectively, validating that the MB, not the Me-4PACz can effectively suppress the Pb^0 (Supplementary Fig. 22 and Fig. 23). In addition, we also can notice that the Pb 4f spectra show a peak shift after incorporating MB, which confirms the interaction between Pb atom and MB molecule, validating the DFT results discussed above in Figure 1g. These results proved that the MB can serve as the redox mediator to suppress the interfacial detrimental reaction through reducing the high-valence-states Ni species ($Ni^{>3+}$) and oxidizing Pb^0, enhancing the interface stability.

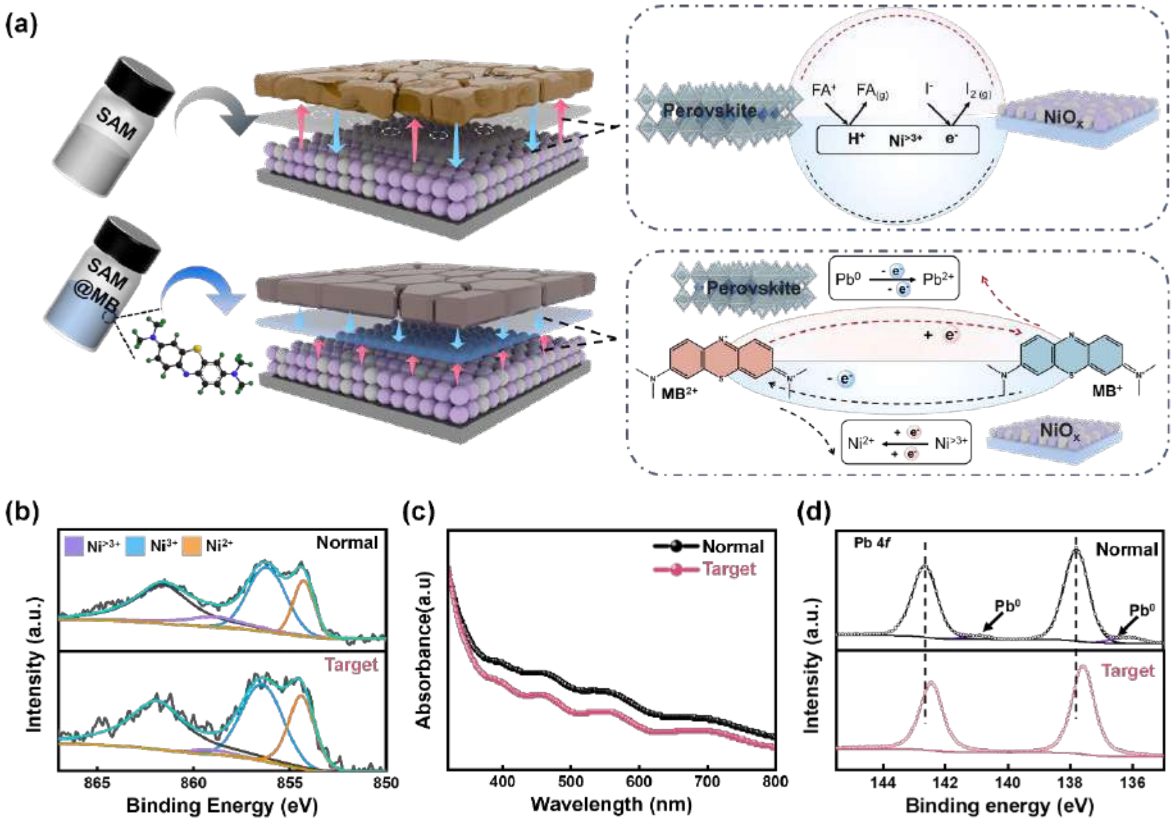

Fig. 3. Inhibition of Interfacial Redox Reactions. (a) Diagram and equations of interfacial redox reactions. (b) Ni 2p spectra of the normal and target SAM (based on the NiO_x layer). (c) UV-vis absorption spectra of normal and target SAM (based on the aged NiO_x layer). (d) Pb 4f spectra of the normal and target perovskite film.

Photovoltaic performance of PSCs

We fabricated PSCs with a structure shown in Supplementary Fig. 2, then evaluated their photovoltaic performance. Firstly, we performed dark current characterization, as illustrated in Figure 4a. The dark saturation current density (J_0) was effectively suppressed in target PSCs, which mainly results from the promoted interfacial hole extraction and reduced non-radiative carrier recombination. The increased recombination resistance calculated from the test of electrochemical impedance spectroscopy (EIS) also validated the reduced carrier recombination after interface modification (Supplementary Fig. 24). Besides, the relationship between V_{OC} and light intensity was investigated according to the equation of $V_{OC}=(n_{ID}k_BT/q)*\ln(I)$ (where k_B is the Boltzmann constant and q is the elementary charge). The ideality factors (n_{ID}) were determined to be 2.32 and 1.46 for normal PSCs and target PSCs, respectively (Figure 4b). A lower n_{ID} indicates reduced trap-assisted recombination within the PSCs, aligning with the results of dark current characterization and EIS test. These above results of inverted PSCs confirm that the

View Article Online
DOI: 10.1039/D4EE05310B

MB can effectively reduce the non-radiative carrier recombination, supporting to improve the efficiency of PSCs.

We prepared 20 target PSCs and 20 normal PSCs, respectively, and then collected their photovoltaic parameters. As illustrated in Figure 4c, the PCE distributions for these PSCs reveal that the average PCE of target PSCs is 25.50%, surpassing that (22.43%) of normal PSCs. Additionally, the statistical analyses of other photovoltaic parameters also carried out (Supplementary Fig. 25), showing that the improvement of PCE after incorporating MB into interfacial layer mainly results from the improved V_{OC} and FF. Notably, as seen in Figure 4d, the target PSCs achieved a maximum PCE of 26.39%, with a short-circuit current density (J_{SC}) of 25.81 mA cm^{-2}, an open-circuit voltage (V_{OC}) of 1.192 V, and a fill factor (FF) of 85.81%. In contrast, the normal PSCs reached a maximum PCE of 24.37%, with a J_{SC} of 25.46 mA cm^{-2}, a V_{OC} of 1.174 V, and an FF of 81.54%. The specific parameters under forward and reverse scan of the champion PSCs were presented in Supplementary Table S1. The external quantum efficiency (EQE) spectra (Figure 4e) were also measured, where the integrated J_{SC} values of both normal and target PSCs show a small variation with those obtained from the *J-V* measurements.

We also fabricated PSCs with an active area of 1 cm². As illustrated in Figure 4f, the target PSCs achieved a maximum PCE of 24.89%, significantly higher than the normal PSCs' PCE of 23.89%. The specific parameters under forward and reverse scans for these PSCs were presented in Supplementary Table S2. Additionally, we produced an additional set of 10 target 1 cm²-PSCs, with their performance parameters presented in Supplementary Table S3, showing an average PCE of 24.39%. These results elucidate the advantageous role of MB molecules in SAM functionalization and interface modification, thereby substantiating the potential and efficacy of MB for fabricating PSCs with large aperture area.

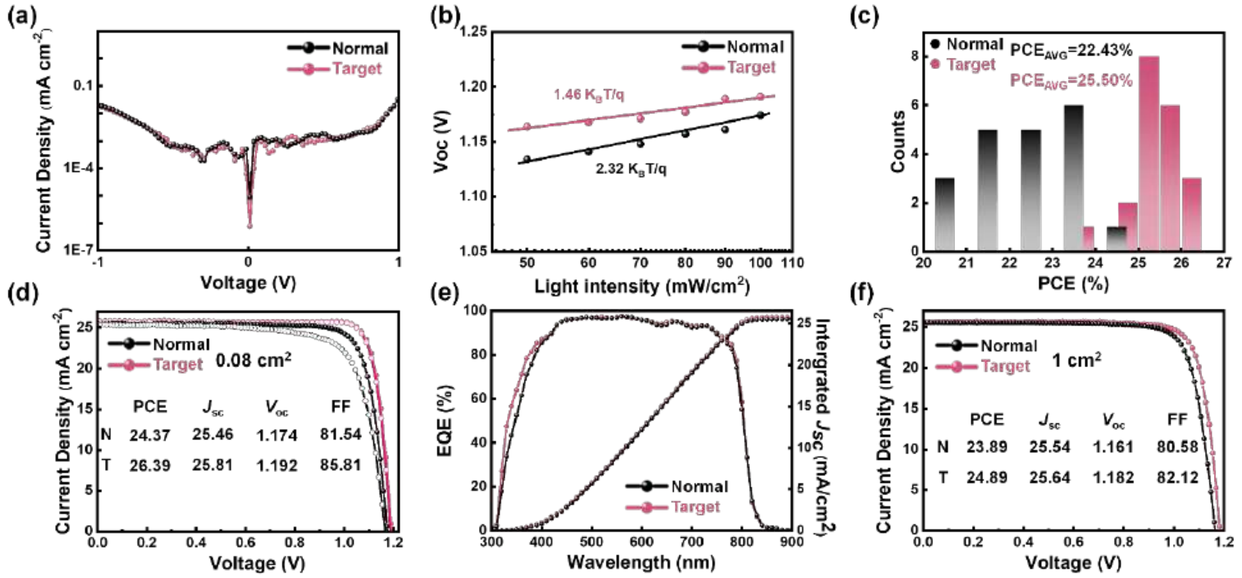

Fig. 4. Photovoltaic performance of normal and target PSCs. (a) Dark *J–V* curves of SAM and SAM with MB based PSCs (b) V_{OC} of PSCs with various SAMs plotted against the logarithm of light intensity (c) Distribution histograms of the PCE values of the 20 normal and target PSCs. (d) *J–V* curves of normal and target PSCs with an active area of 0.08 cm². (e) EQE spectra of the normal and target PSCs. (f) *J–V* curves of normal and target PSCs with an active area of 1 cm².

Enhanced device stability

The MB molecules can effectively reduce the interfacial defects and suppress interfacial redox reactions, which is supposed to enhance device stability. In order to systematically evaluate the stability of perovskite films and the corresponding PSCs, we conducted a series of measurements. First, we assessed the humidity stability of the perovskite films by exposing them to ambient conditions with a relative humidity (RH) of 35% and a temperature of 25 °C for 1000 hours. We investigated the film morphology using SEM measurement. As shown in Figures 5a and 5b, for the perovskite film deposited on the normal SAM, decomposition validated by visible structural changes was observed after storage for 1000 hours. In contrast, the perovskite film deposited on the target SAM shows negligible changes in surface morphology, indicating enhanced stability under the same conditions. We further analyzed the perovskite film at initial and final stages, respectively, using XRD measurements. For the perovskite film deposited on the normal SAM, the (100) peak intensity significantly diminished, while the PbI_2 peak intensity increased after 1000 hours of aging (Figure 5c, Supplementary Fig. 26). This suggests that the perovskite film underwent decomposition under humid conditions. In comparison, the XRD pattern of perovskite film deposited on target SAM shows slight change, indicating that the perovskite film can remain stable after aging in humid air conditions for 1000 hours. Following the evaluation of the improved stability of perovskite film, we proceeded to assess the stability of the device. We placed the devices in an environment with approximately 25% RH and 25 °C, and then monitored their efficiency evolution. After aging for 2016 hours, the target device retained 92% of its initial PCE, whereas the normal device retained only 79% of its initial PCE (Figure 5d). The harsher conditions were applied to accelerate the aging of devices for assessing their stability. First, we placed the devices in a nitrogen glovebox at approximately 50 °C under continuous UV irradiation. It was found that the target device retained 91% of its initial PCE after

View Article Online
DOI: 10.1039/D4EE05310B

1500 hours, whereas the PCE of the normal device rapidly declined to 64% of its initial value (Figure 5e). Additionally, we aged the devices under temperature cycles from 25 °C to 85 °C to 25 °C, in which a cycle lasts for 35 mins [52]. The panel parameters during this process are shown in Supplementary Fig. 27. After 100 cycles, the target device maintained 90% of its initial PCE, while the normal device retained only 79% of its original PCE (Figure 5f). Finally, we conducted long-term operational stability tests on unencapsulated devices under continuous 1-sun illumination in a glovebox, with controlled conditions of 15%RH and a temperature of 45 °C (Figure 5g). Remarkably, the target device retained 90% of its initial PCE after 1500 hours of operation, while the PCE of the normal device significantly dropped after just 425 hours. Based on the above stability analysis, it was evident that utilizing the redox MB to functionalize the SAM interfacial layer can enhance the device stability, which is mainly attributed to the stabilized buried interface from reduced interface defects and suppressed interfacial redox reaction.

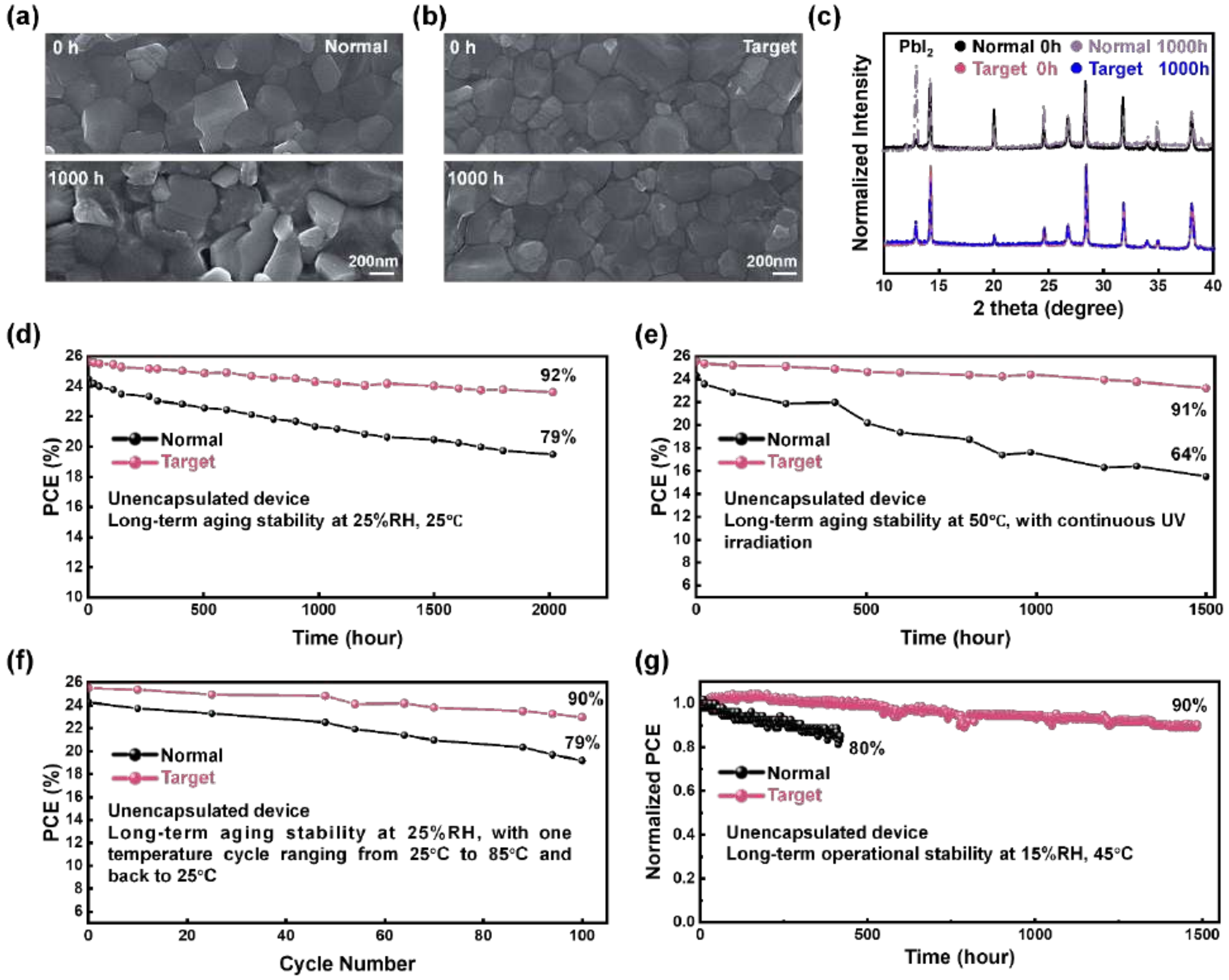

Fig. 5. Accelerated stability tests. (a, b) SEM image of the normal and target films. Both films were stored under ambient conditions with an RH of 35% for 1000 h. (c) XRD spectra of the normal and target films. Both films were stored under ambient conditions with an RH of 35% for 1000 h. (d) Long-term stability of unencapsulated devices stored under ambient conditions of 25% RH and 25 °C. (e) Long-term stability of unencapsulated devices stored under continuous UV irradiation with an intensity of 50 mW/cm^2 in an N_2 glove box. (f) Long-term stability of unencapsulated devices at 25% RH, with temperature cycles ranging from 25 °C to 85 °C and back to 25 °C. (g) Operational stability of the unencapsulated devices under continuous simulated AM1.5 illumination at the maximum power point and approximately 15% RH, 45 ℃ in a glovebox.

Conclusions

In summary, our work demonstrated a redox mediator-functionalized interfacial layer for efficiency improvement and stability enhancement of inverted PSCs. In-depth analysis combining both experimental measurements and theoretical calculations revealed that methylene blue can optimize the Me-4PACz's morphology and electrical properties. Moreover, the methylene blue can also serve as a redox mediator to selectively reduce the high-valence state of Ni species and oxidize metallic Pb^0, while simultaneously passivating interfacial defects. Owing to the promoted interfacial carrier transport and suppressed interfacial detrimental reaction, the PSCs show an impressive efficiency of 26.39% with an aperture area of 0.08 cm^2 and 24.89% with an aperture area of 1 cm^2, respectively. Furthermore, the device can retain 90% of its initial efficiency after 1500 hours of operation under 1-sun illumination, and retain 91% of its initial efficiency exposure to UV irradiation for 1500 hours. Our work presents a valuable reference regarding

View Article Online
DOI: 10.1039/D4EE05319B

interface stability enhancement through optimizing and functionalizing the interfacial layer, which provides more opportunity for facile access to commercially available inverted p-i-n PSCs.

Author contributions

M.L., S.Q., and H.H. conceived the idea. M.L. and H.H. guided the work as supervisors. S.Q. and H.H. did experimental designs, device fabrication, and data analysis. F.Y., Y.L., Q.Z., and C.S. were involved in device fabrication and conducted part of the characterizations. S.D. and L.Y. assisted with XRD, XPS spectra, and KPFM testing. P.C. and Z.L. provided support for characterizing the redox reactions. S.Q. and H.H. drafted the initial version of the manuscript. S.D., L.Y., Z.L., X.A., Z.W., and T.J. contributed to the manuscript revision and language polishing. All authors participated in discussing the results and contributed to revising the manuscript.

Conflicts of interest

There are no conflicts to declare.

Data availability

The data that support the findings of this study are available from the corresponding authors upon request.

Acknowledgements

This work is supported partially by the National Natural Science Foundation of China (Grant nos. 52232008, 52102245, 52072121, 52402254, and 22409061), Beijing Natural Science Foundation (2222076, 2222077), Beijing Nova Program (20220484016), Young Elite Scientists Sponsorship Program by CAST (2022QNRC001), 2022 Strategic Research Key Project of Science and Technology Commission of the Ministry of Education, Huaneng Group Headquarters Science and Technology Project (HNKJ20-H88), State Key Laboratory of Alternate Electrical Power System with Renewable Energy Sources (LAPS2024-05), the Fundamental Research Funds for the Central Universities (2022MS029, 2024MS036, 2022MS02, 2022MS031, 2023MS042, 2023MS047) and the NCEPU "Double First-Class" Program.

Notes and references

1. National Renewable Energy Laboratory Best Research-Cell Efficiency Chart (NREL, 2024); www.nrel.gov/pv/cell-eficiency. Html.
2. Z. Li, B. Li, X. Wu, S.A. Sheppard, S. Zhang, D. Gao, N.J. Long and Z. Zhu, Science, 2022, 376, 416-420.
3. S. Li, Y. Jiang, J. Xu, D. Wang, Z. Ding, T. Zhu, B. Chen, Y. Yang, M. Wei, R. Guo, Y. Hou, Y. Chen, C. Sun, K. Wei, S.M.H. Qaid, H. Lu, H. Tan, D. Di, J. Chen, M. Grätzel, E.H. Sargent and M. Yuan, Nature, 2024, 635, 82–88.
4. Q. Tan, Z. Li, G. Luo, X. Zhang, B. Che, G. Chen, H. Gao, D. He, G. Ma, J. Wang, J. Xiu, H. Yi, T. Chen and Z. He, Nature, 2023, 620, 545-551.
5. S. Li, Y. Xiao, R. Su, W. Xu, D. Luo, P. Huang, L. Dai, P. Chen, P. Caprioglio, K.A. Elmestekawy, M. Dubajic, C. Chosy, J. Hu, I. Habib, A. Dasgupta, D. Guo, Y. Boeije, S.J. Zelewski, Z. Lu, T. Huang, Q. Li, J. Wang, H. Yan, H.-H. Chen, C. Li, B.A.I. Lewis, D. Wang, J. Wu, L. Zhao, B. Han, J. Wang, L.M. Herz, J.R. Durrant, K.S. Novoselov, Z.-H. Lu, Q. Gong, S.D. Stranks, H.J. Snaith and R. Zhu, Nature, 2024. https://doi.org/10.1038/s41586-024-08159-5.
6. H. Chen, C. Liu, J. Xu, A. Maxwell, W. Zhou, Y. Yang, Q. Zhou, A.S.R. Bati, H. Wan, Z. Wang, L Zeng, J. Wang, P. Serles, Y. Liu, S. Teale, Y. Liu, M.I. Saidaminov, M. Li, N. Rolston, S. Hoogland, T. Filleter, M.G. Kanatzidis, B. Chen, Z. Ning and E.H. Sargent, Science, 2024, 384, 189-193.
7. Y.-H. Lin, Vikram, F. Yang, X.-L. Cao, A. Dasgupta, R.D.J. Oliver, A.M. Ulatowski, M.M. McCarthy, X. Shen, Q. Yuan, M.G. Christoforo, F.S.Y. Yeung, M.B. Johnston, N.K. Noel, L.M. Herz, M.S. Islam and H.J. Snaith, Science, 2024, 384, 767-775.
8. Y. Yang, R. Chen, J. Wu, Z. Dai, C. Luo, Z. Fang, S. Wan, L. Chao, Z. Liu and H. Wang, Angew. Chem. Int. Ed., 2024, 63, e202409689.
9. S. Liu, J. Li, W. Xiao, R. Chen, Z. Sun, Y. Zhang, X. Lei, S. Hu, M. Kober-Czerny, J. Wang, F. Ren, Q. Zhou, H. Raza, Y. Gao, Y. Ji, S. Li, H. Li, L. Qiu, W. Huang, Y. Zhao, B. Xu, Z. Liu, H.J. Snaith, N.-G. Park and W. Chen, Nature, 2024, 632, 536-542.
10. C. Li, Y. Zhang, X. Zhang, P. Zhang, X. Yang and H. Chen, Adv. Funct. Mater., 2023, 33, 2214774.
11. Y. Liu, B. Ding, G. Zhang, X. Ma, Y. Wang, X. Zhang, L. Zeng, M.K. Nazeeruddin, G. Yang and B. Chen, Adv. Sci., 2024, 11, 2309111.
12. C.C. Boyd, R.C. Shallcross, T. Moot, R. Kerner, L. Bertoluzzi, A. Onno, S. Kavadiya, C. Chosy, E.J. Wolf, J. Werner, J.A. Raiford, C. de Paula, A.F. Palmstrom, Z.J. Yu, J.J. Berry, S.F. Bent, Z.C. Holman, J.M. Luther, E.L. Ratcliff, N.R. Armstrong and M.D. McGehee, Joule, 2020, 4, 1759-1775.
13. T. Guo, Z. Fang, Z. Zhang, Z. Deng, R. Zhao, J. Zhang, M. Shang, X. Liu, Z. Hu, Y. Zhu and L. Han, J. Energy Chem., 2022, 69, 211-220.
14. Y. Jin, H. Feng, Y. Li, H. Zhang, X. Chen, Y. Zhong, Q. Zeng, J. Huang, Y. Weng, J. Yang, C. Tian, J. Zhang, L. Xie and Z. Wei, Adv. Energy Mater., 2024, 2403911.
15. N. Yan, Y. Cao, Z. Jin, Y. Liu, S. Liu, Z. Fang and J. Feng, Adv. Mater., 2024, 36, 2403682.
16. Q. Cao, T. Wang, X. Pu, X. He, M. Xiao, H. Chen, L. Zhuang, Q. Wei, H.L. Loi, P. Guo, B. Kang, G. Feng, J. Zhuang, G. Feng, X. Li and F. Yan, Adv. Mater., 2024, 36, 2311970.
17. S. Yu, Z. Xiong, H. Zhou, Q. Zhang, Z. Wang, F. Ma, Z. Qu, Y. Zhao, X. Chu, X. Zhang and J. You, Science, 2023, 382, 1399-1404.

18. Z. Li, X. Sun, X. Zheng, B. Li, D. Gao, S. Zhang, X. Wu, S. Li, J. Gong, J.M. Luther, Z. Li and Z. Zhu, Science, 2023, 382, 284-289.
19. R. Guo, X. Wang, X. Jia, X. Guo, J. Li, Z. Li, K. Sun, X. Jiang, E. Alvianto, Z. Shi, M. Schwartzkopf, P. Müller-Buschbaum and Y. Hou, Adv. Energy Mater., 2023, 13, 2302280.
20. X. Wang, J. Li, R. Guo, X. Yin, R. Luo, D. Guo, K. Ji, L. Dai, H. Liang, X. Jia, J. Chen, Z. Jia, Z. Shi, S. Liu, Y. Wang, Q. Zhou, T. Wang, G. Pan, P. Müller-Buschbaum, S.D. Stranks and Y. Hou, Nat. Photonics, 2024, 18, 1269-1275.
21. M. Liu, L. Bi, W. Jiang, Z. Zeng, S.W. Tsang, F.R. Lin and A.K.Y. Jen, Adv. Mater., 2023, 35, 2304415.
22. D. Li, Q. Lian, T. Du, R. Ma, H. Liu, Q. Liang, Y. Han, G. Mi, O. Peng, G. Zhang, W. Peng, B. Xu, X. Lu, K. Liu, J. Yin, Z. Ren, G. Li and C. Cheng, Nat. Commun., 2024, 15, 7605.
23. Y. Zhou, X. Huang, J. Zhang, L. Zhang, H. Wu, Y. Zhou, Y. Wang, Y. Wang, W. Fu and H. Chen, Adv. Energy Mater., 2024, 14, 2400616.
24. B. Li, C. Zhang, D. Gao, X. Sun, S. Zhang, Z. Li, J. Gong, S. Li and Z. Zhu, Adv. Mater., 2024, 36, 2309768.
25. J. Cao, Q. Chen, W. Wu, J. Fu, Z. Zhang, L. Chen, R. Wang, W. Yu, L. Wang, X. Nie, J. Zhang, Y. Zhou, B. Song and Y. Li, Energy Environ. Sci., 2024, 17, 3454-3469.
26. H. Tan, A. Jain, O. Voznyy, X. Lan, F.P. García de Arquer, J.Z. Fan, R. Quintero-Bermudez, M. Yuan, B. Zhang, Y. Zhao, F. Fan, P. Li, L.N. Quan, Y. Zhao, Z.-H. Lu, Z. Yang, S. Hoogland and E.H. Sargent, Science, 2017, 355, 722-726.
27. H. Min, D.Y. Lee, J. Kim, G. Kim, K.S. Lee, J. Kim, M.J. Paik, Y.K. Kim, K.S. Kim, M.G. Kim, T.J. Shin and S.I. Seok, Nature, 2021, 598, 444-450.
28. S.M. Park, M. Wei, N. Lempesis, W. Yu, T. Hossain, L. Agosta, V. Carnevali, H.R. Atapattu, P. Serles, F.T. Eickemeyer, H. Shin, M. Vafaie, D. Choi, K. Darabi, E.D. Jung, Y. Yang, D.B. Kim, S.M. Zakeeruddin, B. Chen, A. Amassian, T. Filleter, M.G. Kanatzidis, K.R. Graham, L. Xiao, U. Rothlisberger, M. Grätzel and E.H. Sargent, Nature, 2023, 624, 289-294.
29. X. Chu, Q. Ye, Z. Wang, C. Zhang, F. Ma, Z. Qu, Y. Zhao, Z. Yin, H.X. Deng, X. Zhang and J. You, Nat. Energy, 2023, 8, 372-380.
30. S. Tan, T. Huang, I. Yavuz, R. Wang, T.W. Yoon, M. Xu, Q. Xing, K. Park, D.-K. Lee, C.-H. Chen, R. Zheng, T. Yoon, Y. Zhao, H.-C. Wang, D. Meng, J. Xue, Y.J. Song, X. Pan, N.-G. Park, J.-W. Lee and Y. Yang, Nature, 2022, 605, 268-273.
31. Z. Lan, H. Huang, Y. Lu, S. Qu, M. Wang, S. Du, Y. Yang, C. Sun, Q. Zhang, Y. Suo, X. Wang, L. Yan, P. Cui, Z. Zhao and M. Li, Adv. Funct. Mater., 2024, 34, 2316591.
32. C. Li, L. Chen, F. Jiang, Z. Song, X. Wang, A. Balvanz, E. Ugur, Y. Liu, C. Liu, A. Maxwell, H. Chen, Y. Liu, Z. Wang, P. Xia, Y. Li, S. Fu, N. Sun, C.R. Grice, X. Wu, Z. Fink, Q. Hu, L. Zeng, E. Jung, J. Wang, S.M. Park, D. Luo, C. Chen, J. Shen, Y. Han, C.A.R. Perini, J.-P. Correa-Baena, Z.-H. Lu, T.P. Russell, S. De Wolf, M.G. Kanatzidis, D.S. Ginger, B. Chen, Y. Yan and E.H. Sargent, Nat. Energy, 2024, 1–9. https://doi.org/10.1038/s41560-024-01613-8.

33. R. He, W. Wang, Z. Yi, F. Lang, C. Chen, J. Luo, J. Zhu, J. Thiesbrummel, S. Shah, K. Wei, Y. Luo, C. Wang, H. Lai, H. Huang, J. Zhou, B. Zou, X. Yin, S. Ren, X. Hao, L. Wu, J. Zhang, J. Zhang, M. Stolterfoht, F. Fu, W. Tang and D. Zhao, Nature, 2023, 618, 80-86.
34. Y. Zhao, X. Luan, L. Han and Y. Wang, Adv. Funct. Mater., 2024, 2405646. https://doi.org/10.1002/adfm.202405646.
35. C. Fei, A. Kuvayskaya, X. Shi, M. Wang, Z. Shi, H. Jiao, T.J. Silverman, M. Owen-Bellini, Y. Dong, Y. Xian, R. Scheidt, X. Wang, G. Yang, H. Gu, N. Li, C.J. Dolan, Z.J.D. Deng, D.N. Cakan, D.P. Fenning, Y. Yan, M.C. Beard, L.T. Schelhas, A. Sellinger and J. Huang, Science, 2024, 384, 1126-1134.
36. G. Qu, S. Cai, Y. Qiao, D. Wang, S. Gong, D. Khan, Y. Wang, K. Jiang, Q. Chen, L. Zhang, Y.G. Wang, X. Chen, A.K.-Y. Jen and Z.X. Xu, Joule, 2024, 8, 2123-2134.
37. A.R. Pininti, A.S. Subbiah, C. Deger, I. Yavuz, A. Prasetio, P. Dally, V. Hnapovskyi, A.A. Said, L.V.T. Merino, S. Mannar, S. Zhumagali, B. Vishal, M. Marengo, A. Razzaq, M. Babics, T.G. Allen, E. Aydin, R. Azmi and S.D. Wolf, Adv. Energy Mater., 2024, 2403530. https://doi.org/10.1002/aenm.202403530.
38. X. Zhao, Y. Qiu, M. Wang, D. Wu, X. Yue, H. Yan, B. Fan, S. Du, Y. Yang, Y. Yang, D. Li, P. Cui, H. Huang, Y. Li, N.G. Park and M. Li, ACS Energy Lett., 2024, 9, 2659−2669.
39. S. Du, H. Huang, Z. Lan, P. Cui, L. Li, M. Wang, S. Qu, L. Yan, C. Sun, Y. Yang, X. Wang and M. Li, Nat. Commun., 2024, 15, 5223.
40. M. Li, B. Jiao, Y. Peng, J. Zhou, L. Tan, N. Ren, Y. Ye, Y. Liu, Y. Yang, Y. Chen, L. Ding and C. Yi, Adv. Mater., 2024, 36, 2406532.
41. Z. Huang, Y. Bai, X. Huang, J. Li, Y. Wu, Y. Chen, K. Li, X. Niu, N. Li, G. Liu, Y. Zhang, H. Zai, Q. Chen, T. Lei, L. Wang and H. Zhou, Nature, 2023, 623, 531-537.
42. H. Huang, P. Cui, Y. Chen, L. Yan, X. Yue, S. Qu, X. Wang, S. Du, B. Liu, Q. Zhang, Z. Lan, Y. Yang, J. Ji, X. Zhao, Y. Li, X. Wang, X. Ding and M. Li, Joule, 2022, 6, 2186-2202.
43. L. Yan, H. Huang, P. Cui, S. Du, Z. Lan, Y. Yang, S. Qu, X. Wang, Q. Zhang, B. Liu, X. Yue, X. Zhao, Y. Li, H. Li, J. Ji and M. Li, Nat. Energy, 2023, 8, 1158-1167.
44. P. Shi, Y. Ding, B. Ding, Q. Xing, T. Kodalle, C.M. Sutter-Fella, I. Yavuz, C. Yao, W. Fan, J. Xu, Y. Tian, D. Gu, K. Zhao, S. Tan, X. Zhang, L. Yao, P.J. Dyson, J.L. Slack, D. Yang, J. Xue, M.K. Nazeeruddin, Y. Yang and R. Wang, Nature, 2023, 620, 323-327.
45. Y. Yang, Q. Chang, Y. Yang, Y. Jiang, Z. Dai, X. Huang, J. Huo, P. Guo, H. Shen, Z. Liu, R. Chen and H. Wang, J. Mater. Chem. A, 2023, 11, 16871-16877.
46. Y. Zou, W. Yu, H. Guo, Q. Li, X. Li, L. Li, Y. Liu, H. Wang, Z. Tang, S. Yang, Y. Chen, B. Qu, Y. Gao, Z. Chen, S. Wang, D. Zhang, Y. Chen, Q. Chen, S.M. Zakeeruddin, Y. Peng, H. Zhou, Q. Gong, M. Wei, M. Grätzel and L. Xiao, Science, 2024, 385, 161-167.

View Article Online
DOI: 10.1039/D4EE05319B

47. C. Ma, F.T. Eickemeyer, S.H. Lee, D.H. Kang, S.J. Kwon, M. Grätzel and N.G. Park, Science, 2023, 379, 173-178.
48. Y. Li, S. Yuan, S. Miao, J. Wu, H.Y. Wang, Y. Wang, X.C. Ai and J.P. Zhang, J. Phys. Chem. C, 2023, 127, 14679-14686.
49. R. Islam, G. Chen, P. Ramesh, J. Suh, N. Fuchigami, D. Lee, K.A. Littau, K. Weiner, R.T. Collins and K.C. Saraswat, ACS Appl. Mater. Interfaces, 2017, 9, 17201–17207.
50. S. Wu, Y. Yan, J. Yin, K. Jiang, F. Li, Z. Zeng, S.W. Tsang and A.K.Y. Jen, Nat. Energy, 2024, 9, 411–421.
51. X. Huang, L. Bi, Z. Yao, Q. Fu, B. Fan, S. Wu, Z. Su, Q. Feng, J. Wang, Y. Hong, M. Liu, Y. An, M. Chen and A.K.Y. Jen, Adv. Mater., 2024, 36, 2410564.
52. Q. Zeng, H. Xiao, Q. Ma, R. Huang, Y. Pan, L. Li, X. Liao, S. Liu, W. Zhang and F. Liu, Adv. Energy Mater., 2024, 14, 2401279.

View Article Online
DOI: 10.1039/D4EE05319B

Data availability statements:

The data supporting this article have been included as part of the Supplementary Materials.